Soot Morphology and Nanostructure Differences between Chinese Aviation Kerosene and Algae-Based Aviation Biofuel in Free Jet Laminar Diffusion Flames

Di Chang, Jiacheng Li, Yiyang Yang, and Zhiwen Gan*

Read Online

ACCESS | Metrics & More | Article Recommendations

ABSTRACT: Aircraft soot has a significant effect on the air quality and human health. The aim of this study is to investigate the evolution of soot morphology in free jet laminar diffusion flames between Chinese traditional aviation kerosene RP-3 and algae-based aviation biofuels. The differences in height, profile, and structural properties of soot between the RP-3 flame and biofuel flame are determined. A laboratory-made probe sampling method was applied for soot sample collection. Transmission electron microscopy (TEM), high-resolution transmission electron microscopy (HRTEM), X-ray diffraction (XRD), and elemental analyzers were used to analyze the collected soot particles. The average particle size of soot increases first and then decreases in both flames, and the size of biofuel primary particles is smaller than that of jet fuel RP-3 particles along the same flame height. At the flame tip, the primary particle sizes of RP-3 soot and biofuel soot are 22.7 and 15.6 mm, respectively. In comparison with the RP-3 soot, the nanostructure of biofuel soot particles along the same flame height exhibits a shorter fringe lattice, a larger fringe tortuosity, and a larger interlayer spacing, which indicate a higher degree of oxidation reactivity. Meanwhile, RP-3 soot particles have a lower H/C atom ratio and have greater intensity in X-ray diffraction, which indicates a more orderly and compact lattice structure. This study provides some references in studying the algae-based biofuel with regard to soot formation.
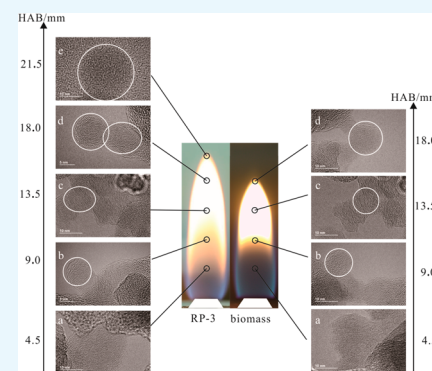
1. INTRODUCTION

Aircraft soot has a significant effect on air pollution and the global environment. With concerns ranging from climate change to the security of fuel supplies, algae-based aviation biofuels are receiving increasing attention. Recent studies have indicated that algae-based biofuel has a higher energy return than fossil fuel.[1] In recent years, algae-based biofuel has received extensive attention due to its relatively good combustion performance and environmentally friendly characteristics. In addition, this renewable feature of algae-based biofuel may bring a potential solution to carbon emission issues.[1,2]

Soot formation is a major branch in the field of fuel combustion. Glassman et al. proposed a classic theory of soot formation for hydrocarbon fuels.[3] It has been shown that the soot formation process undergoes several major stages. Pyrolysis of hydrocarbon fuel first produces some small hydrocarbon molecules. Then those small hydrocarbon molecules form a benzene ring. After that, two or more benzene rings form a polycyclic aromatic hydrocarbon (PAH). PAHs will nucleate when they reach a certain stage of growth. They continually grow in volume and form into soot by undergoing a process of surface growth, oxidation, and particle collision.

There are various aspects in the study of soot formation. Some scholars have studied the soot precursors, which are also called polycyclic aromatic hydrocarbons (PAHs), before the soot is mature.[4,5] Some researchers focused on the chemical reaction mechanism of soot formation. Others focused on the soot morphology investigation in the soot formation process for a laboratory-scale flame configuration. Morphology parameters describing soot include primary particle diameter, nanostructure characteristics, etc. The nanostructure parameters, including lattice fringe length, fringe curvature, and interlayer spacing, reflect the oxidative reactivity of soot particles to a certain extent.[6−14]

Liati[15] et al. observed the microscopic morphology of soot particles from the exhaust of a military engine between standard kerosene and a biofuel blend. More uncrystallized layers in the outer boundary of the biofuel blend soot indicate a higher degree of oxidative reactivity. In 2011, Blakey et al.[16]

applied a hybrid fuel of traditional aviation kerosene and aviation biofuel to an aero engine, which had a significant effect in reducing the emission of soot particles. Many previous works that have investigated soot characterization from aircraft engine exhaust with biofuel blends have concluded that alternative fuels reduce soot emissions. However, few studies mention the soot formation in the actual combustion chamber, as the actual combustion chamber combustion is complex. It is difficult to study the actual soot formation process in practical chamber combustion. As a result, it is particularly important to study soot formation process under laboratory-scale configurations. As a significant branch of soot formation in combustion research, soot formation characteristics for one laboratory-scale reaction configuration (e.g., nonpremixed flames, laminar premixed flame, shock tubes, and flow reactors) have been studied by many scholars.[13,17−21] However, these studies mostly focused on the soot nanostructure characteristics for methane, ethylene,[17−20] aviation fuel,[13,21] and so on. A nanostructure characteristics study on soot formation formed by an algae-based aviation biofuel has yet to be presented. It is also significant to study the effects of an algae-based biofuel on the soot generation in a laboratory-scale flame. Understanding the effects of the components of algae-based biofuel on the soot nanostructure characteristics will provide some insights into the design of cleaner and more efficient engines.

In this study, two kinds of fuels, algae-based aviation biofuels and Chinese standard jet fuel RP-3, were applied for a free jet laminar diffusion flame experiment. A comparison of the evolution of soot morphology between the RP-3 flame and the biofuel flame was carried out. Particle collection along the central axis of the flames used a method of laboratory-made probe sampling. Transmission electron microscopy (TEM), high-resolution transmission electron microscopy (HRTEM), X-ray diffraction (XRD), and elemental analysis were utilized to compare the differences in soot morphologies and soot evolution processes between the two different fuels on a microscopic scale. The aim of this paper is to evaluate the significance of algae-based biofuels in fulfilling higher emission requirements in practical combustion devices by comparing the different morphology characteristics of soot particles between RP-3 fuel and biomass fuel.

2. RESULTS AND DISCUSSION

Figure 1 shows the TEM images of soot particles collected at different heights of two fuel flames. A clear boundary can be observed from soot collected at 4.5 mm height above the burner (HAB) in RP-3 flame. As the flame height increases, the group of soot particles develops from the initial chain region to the later flake region due to particle aggregation. Observations of the particle morphology in the biomass flame show that there is no clear boundary at 4.5 mm HAB and the contribution has a more amorphous liquidlike structure. Particles collected after the biofuel flame height of 9 mm can be seen to have a clear boundary, and as the flame height increases, particles gradually develop from the chain region to the flake region.

Figure 2 manifests the variation of soot particle size along the flame centerline. The average primary particle size of each sampling point is derived from the TEM images processed by software the Image-Pro Plus (IPP). At each sampling point, 80−100 soot particles were selected for s quantitative size analysis, and the arithmetic mean value of this large group of
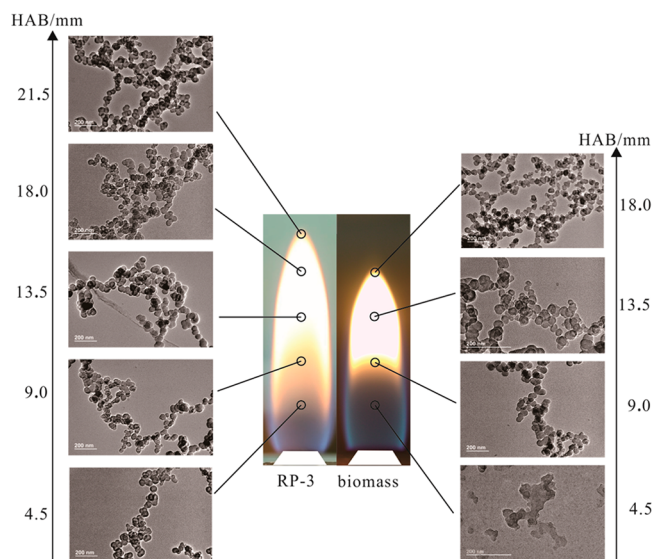
Figure 1. TEM images of soot particles along different flame heights of RP-3 (left) and biofuel (right).
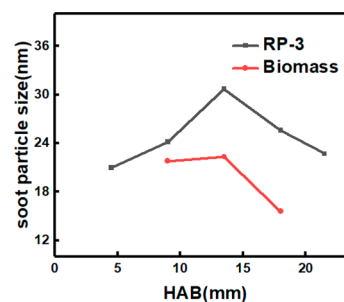
Figure 2. Variation of soot particle size along the flame centerline.

particle sizes was regarded as the average primary particle size of each point.

The size of soot particles changes continuously during the combustion process, and the basic particle size is mainly affected by the oxidation reaction and surface growth of soot particles.[22,23] The soot particles are mainly grown through an H atom abstraction and acetylene addition (HACA mechanism) reaction on the surface of the particles, PAHs condensation, and particle agglomeration.[24] As the flame height increases, the soot particle size increases at first and then decreases, as shown in Figure 2. The reason is that the surface growth rate of particles is greater than the oxidation reaction rate at a relatively lower flame height while the oxidation rate of soot is greater than the surface growth rate at a relatively higher flame height. In addition, the soot particle size of the RP-3 flame is larger than that of the biofuel flame at the same flame height.

To verify the repeatability of the soot sampling, sampling was performed for each sampling point at least twice. These results agreed well with each other. For instance, Figure 3 shows the histograms of the soot particle sizes and their fitted curves for two samplings at 18.0 mm HAB of the RP-3 flame. It can be seen from Figure 3 that the trends of the histogram distributions in two samplings are roughly consistent. The average particle sizes of the soot in the two samplings are 25.52 and 25.49 nm, respectively. The difference is far less than the standard error.
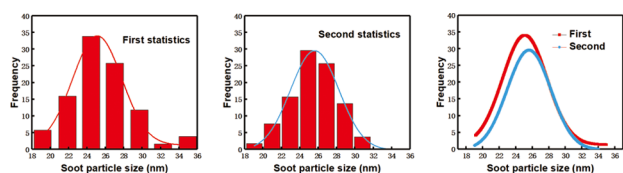
Figure 3. Comparison of the two samplings for RP-3 at h = 18.0 mm.

2.1. Flame Shape. Figure 4 gives a picture of the laminar flames of the two fuels. The RP-3 flame is on the left side of

Figure 4. Different fuel flames (RP-3 flame on the left and biomass flame on the right).

the picture, and the biomass fuel is on the right side of the picture. The RP-3 flame is higher and brighter than the biomass flame, and both are in the shape of a candle flame.

2.2. Soot Nanostructure. The characteristics of the internal carbon lamella (i.e., layers) comprising a soot primary particle are collectively called the nanostructure. The soot nanostructure is a function of formation conditions of time, temperature, and fuel molecular structure/composition.[24,25] The soot nanostructure reflects not only the physical form of soot segment distribution but also the oxidative activity and degree of graphitization.

Figure 5 shows the HRTEM images of soot and the skeletonized images processed with the software ImageJ. Figure 5a,b are the skeletonized images of RP-3 soot (HAB = 18.0 mm) and biofuel soot (HAB = 18.0 mm) respectively.
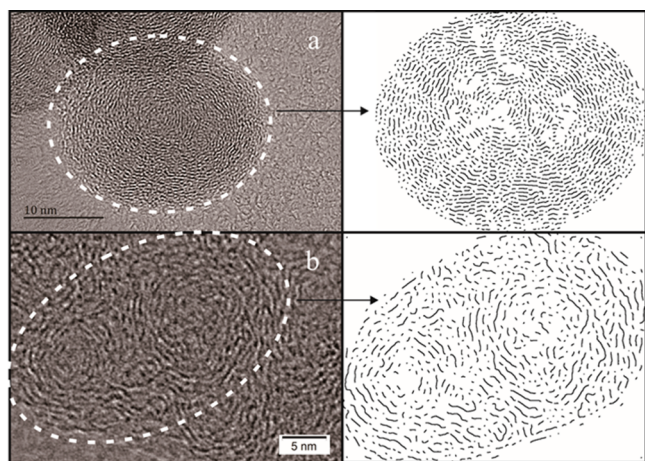
Figure 5. HRTEM image processing result ((a) nanostructure of RP-3 soot (HAB = 18.0 mm) (b) nanostructure of biomass soot (HAB = 18.0 mm)).

Figure 6 shows the nanostructures of soot particles at five heights in the RP-3 diffusion flame. As the flame height
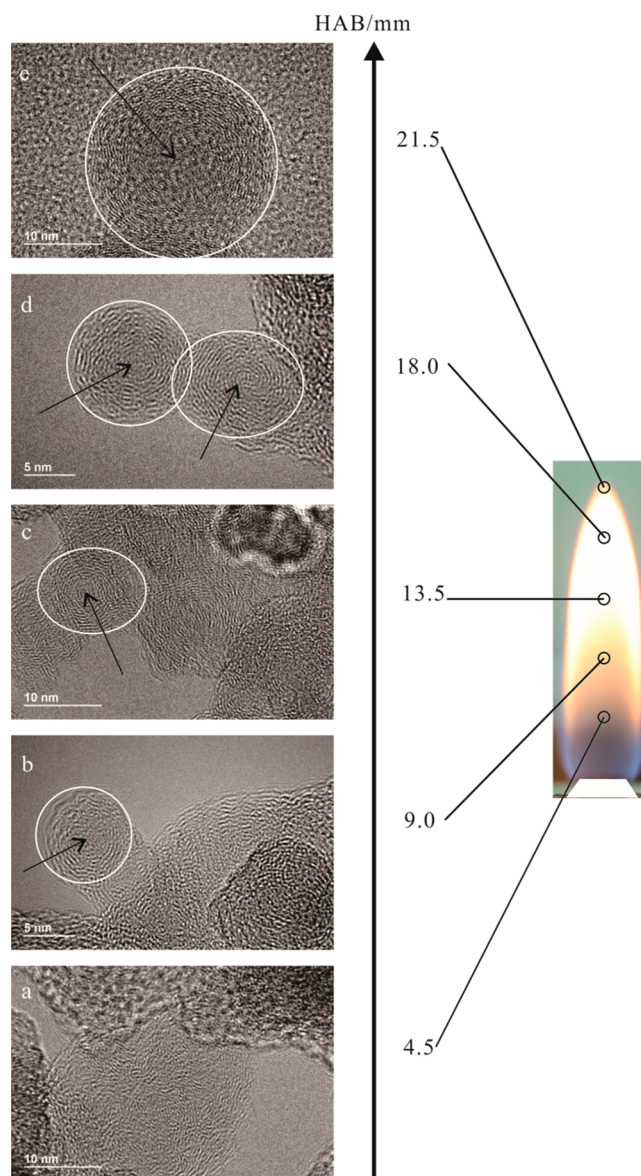
Figure 6. HRTEM images of RP-3 soot sampled at (a) HAB = 4.5 mm, (b) HAB = 9.0 mm, (c) HAB = 13.5 mm, (d) HAB = 18.0 mm, and (e) HAB = 21.5 mm.

increases, the crystallinity of the soot particles increases. At 4.5 mm HAB, the soot structure is amorphous. It exhibits lamellae with an incoherent orientation and no obvious single center of a concentric shell. From 9.0 to 21.5 mm, the soot particles have an onion core−shell structure and show a more instinct single center (black arrows in Figure 6b−e). The lattice fringe is more distinct with the height increase because of the condensation of PAHs and the surface growth of soot particles. At 18.0 mm HAB, an evident center can be noted corresponding to an amorphous and uniform appearance (marked by black arrows in Figure 6d). The overall structural distribution of the particles is that the external carbon layer is ordered with an oriented shell and the interior is an amorphous carbon core. The ordered aromatic layers constitute the concentric external shells and the amorphous

aromatic hydrocarbons constitute the internal disordered structure.[26,27] From HAB = 18.0 mm to HAB = 21.5 mm, extended graphene layers with more organized outer fringes around the nuclei and distinct boundaries (Figure 6d,e) are observed in soot particles.

Figure 7 presents the HRTEM images of biofuel soot particles. At an HAB of 4.5 mm (Figure 7a), the particles have
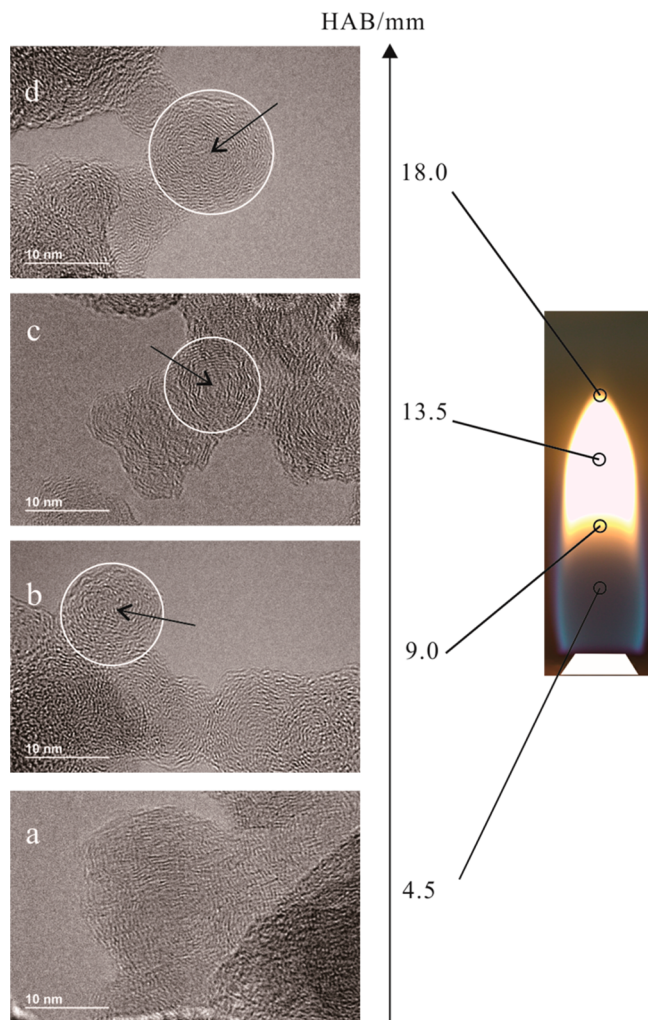
Figure 7. HRTEM images of biofuel soot sampled at (a) HAB = 4.5 mm, (b) HAB = 9 mm, (c) HAB = 13.5 mm, and (d) HAB = 18.0 mm

an overall amorphous structure and no oriented carbon layers and a distinct core can be observed. Soot particles exhibited no recognizable lamellae with negligible curvature and orientation in the nanostructure. At 9.0 mm HAB, some particles show a certain degree of graphitization. A typical core–shell structure has emerged (Figure 7b). As the soot particles continue to develop in the flame, increasingly more stacking and clear graphene layers can be observed (Figure 7c,d). At 18.0 mm HAB, the primary particles appear larger, as shown in Figure 7d, including larger areas of external concentric carbon layers and smaller areas of an internal amorphous carbon core (the disordered cores are marked by arrows in Figure 7b−d). At the flame tip, the biofuel soot appears to have shorter fringe lengths and a smaller radius of curvature in comparison to the RP-3 soot, indicating a lower degree of graphitization.

In addition, at 4.5 mm HAB of both fuel flames corresponding to initial stage of the combustion, some liquidlike particles are observed at this sampling point. Most of the soot particles have an amorphous structure at this sampling point. Most particles have not yet undergone the transformation of particle inception at this early stage. Thus, structural parameters were not derived at this sampling point in both flames. This sampling point (4.5 mm HAB) for both fuels will not be introduced in the following discussion about the parameters of soot nanostructure.

Figure 8 plots the histograms of the fringe length, layer spacing, and fringe tortuosity of the soot particles in the RP-3 flame at different flame heights. Fringes shorter than an aromatic ring (i.e., 0.246 nm) are first eliminated, since they make no physical sense.[27] Related studies and carbon theory give the following facts.

Figure 8a shows that soot derived from a higher flame height corresponds to a larger fringe length of the nanostructure. Carbon atoms located at the edges and carbon atoms located at the interior constitute a carbon layer. The reactivity of the carbon atoms at the edges is far higher than that of the carbon atoms at the center of the layer.[25,28,29] The longer fringe lattice means that a larger proportion of less reactive carbon atoms are located inside the carbon layer. Consequently, as the flame height increases, the nanostructure of soot particles exhibits more longer fringe lattices, which indicate a lower oxidation activity.

In the TEM image analysis, the lamellae with a carbon layer spacing of greater than 0.6 nm (after which van der Waals forces are ignorable)[17,27,30] and smaller than 0.2 nm[31] (the fringe information is attenuated if the fringe spacing is 0.21 nm or less) were excluded. The carbon layer spacing has a certain range because the highly graphitized carbon interlayer spacing is 0.344 nm[32] and the carbon layer spacing that is analyzed should fall within that range. The above selection rules ensure that the collected interlayer spacing results are not distorted. Figure 8b plots the histograms of the layer spacing. As the height of the particle soot rises with the flame, the interlayer spacing decreases from 0.39 nm at 4.5 mm HAB to 0.35 nm at the flame tip. The larger carbon layer spacing is conducive to the entry of oxygen, and the carbon atoms at the edge of the carbon layer are prone to an oxidation reaction, which enhances the reactivity of graphene crystallites.[28] Therefore, as the flame height increases, the soot exhibits more stacked layers and less oxidation, which confirms that the soot has a higher graphitization.

As shown in Figure 8c, the fringe tortuosity of the soot nanostructure gradually decreases as the flame height increases because of the bending phenomenon, which indicates an orderly structure. This bending phenomenon is caused by the odd-membered carbon rings on the carbon layer. Odd-membered carbon rings (i.e., C5 and C7) and higher sp^3 hybridization rates indicate that the carbon layer is more curved and unstable.[29] This suggests that the soot particles are more prone to an oxidation reaction.[33]

Figure 9 shows the histograms of fringe length, layer spacing, and fringe tortuosity of the soot particles in the biofuel flame at HAB = 4.5, 9.0, 13.5, 18.0 mm. Figures 8 and 9 show that the histogram distribution of the nanostructure parameters has a roughly normal distribution, and there is no obvious visual difference. As the soot particles travel through the flame, they exhibit greater fringe length and smaller fringe tortuosity and interlayer spacing, indicating a more orderly structure.
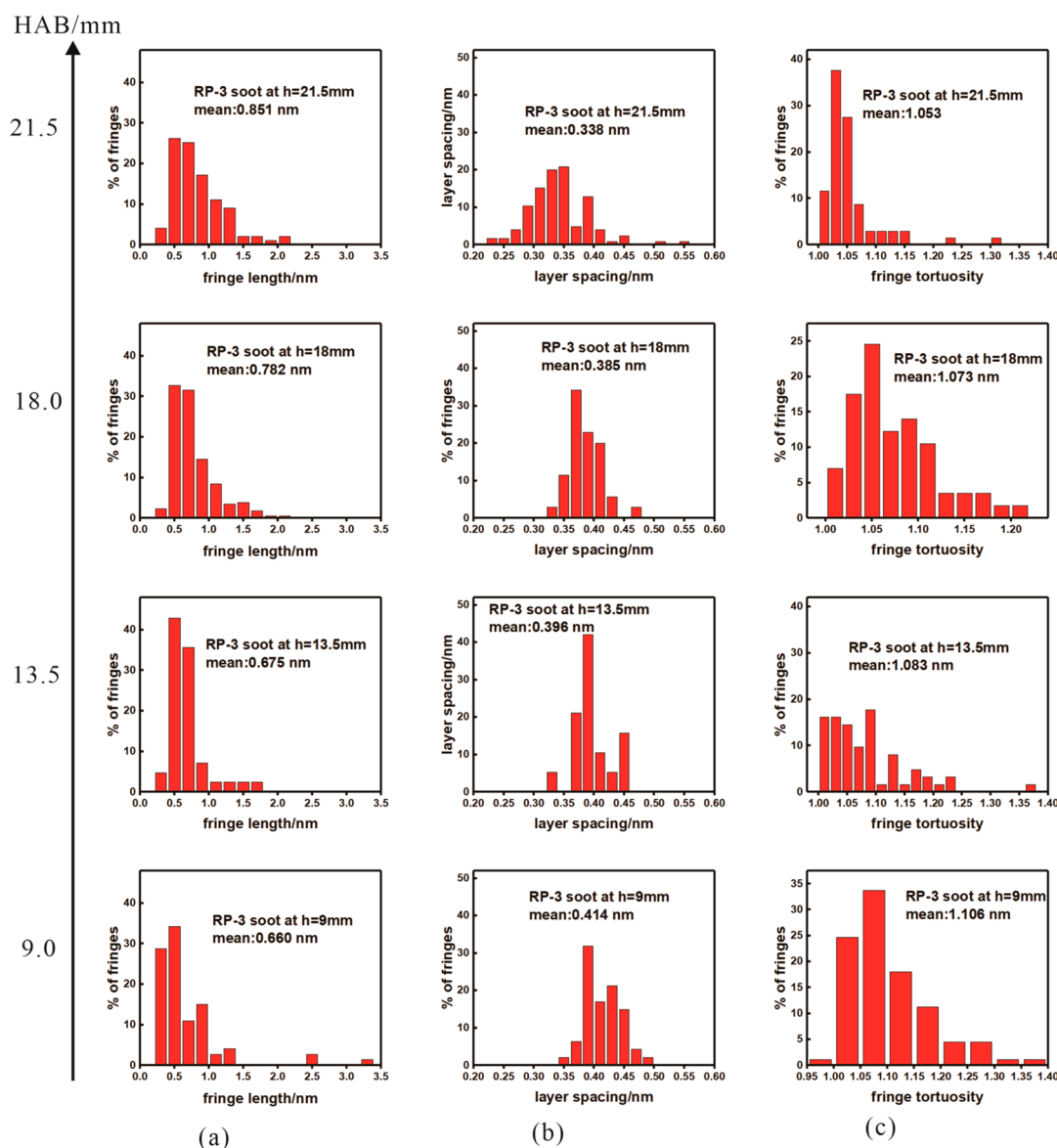
Figure 8. Histograms of (a) fringe length, (b) layer spacing, and (c) fringe tortuosity of RP-3 soot at different HABs.

Figure 10 shows the nanostructure parameters of soot collected at different sampling points in the RP-3 flame and biofuel flame. It also shows that the RP-3 soot exhibits a more orderly structure in comparison with biofuel soot. A reasonable explanation is that a higher concentration of aromatic components in RP-3 aviation kerosene provides an environment conducive to soot precursor (PAH) formation, which contributes to the rapid soot generation.[27,34,35]

2.3. X-ray Diffraction. An X-ray diffraction analysis (XRD) was applied to compare the nanostructure differences between the RP-3 soot and biomass soot in a different way and to validate the results of the HRTEM analysis at the same time. The XRD analysis of the soot particles at the same sampling point of the two fuel flames is shown in Figure 11.

This method has been extensively applied to previous studies on soot.[36] The 2θ values of the two peaks are at 23° (002 plane) and 44° (100 plane) were observed, which are related to the interlayer spacing of the carbon layer and the lateral extension of the carbon plane, respectively. The relatively higher intensity of the 100 and 002 peaks of RP-3

soot particles indicates a higher degree of graphene layer stacking and a greater nanocrystallite width and hence a more compact soot structure. Figure 11 confirms that soot of the RP-3 flame is more mature than that of biofuel flame. The results are consistent with the conclusions about soot HRTEM analysis.

2.4. Elemental Analysis. Table 1 gives a comparison of the elemental content of soot particles generated by the two different fuel flames. According to the information shown in Table 1, the components of both fuel soot particles includes C, H, and O elements with over 90% contents of C. In comparison with RP-3 soot, the relatively lower content of C and relatively higher content of O of biofuel soot may be caused by the content of carboxylic acids, aldehydes, ketones, alcohols, and other substances in biofuel.[37] A relevant study[38,39] pointed out that the hydrogen content is related to the solid active site, and the active site is involved in the reaction to give O_2 and CO_2. The results of an elemental analysis in this experiment coincide well with those of a previous study[27] that the reduction of H/C means an increase
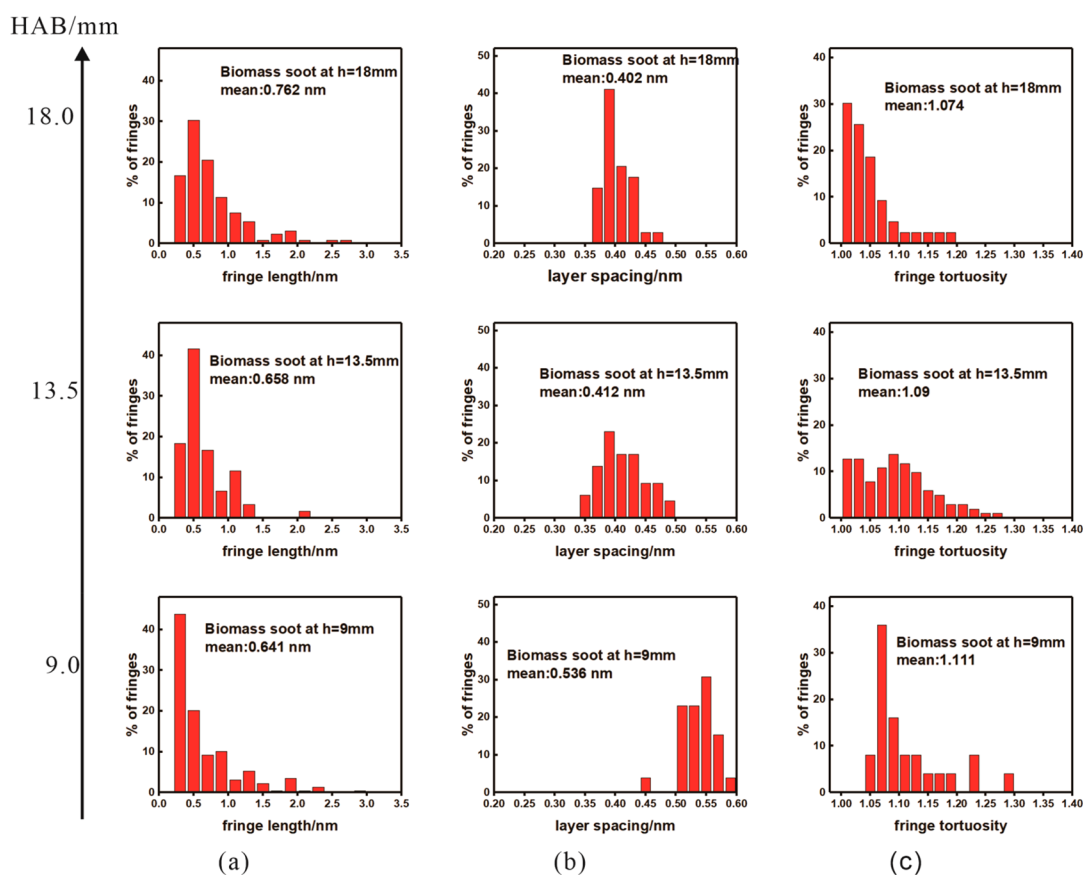
Figure 9. Histograms of (a) fringe length, (b) layer spacing, and (c) fringe tortuosity of biofuel soot at different HABs.
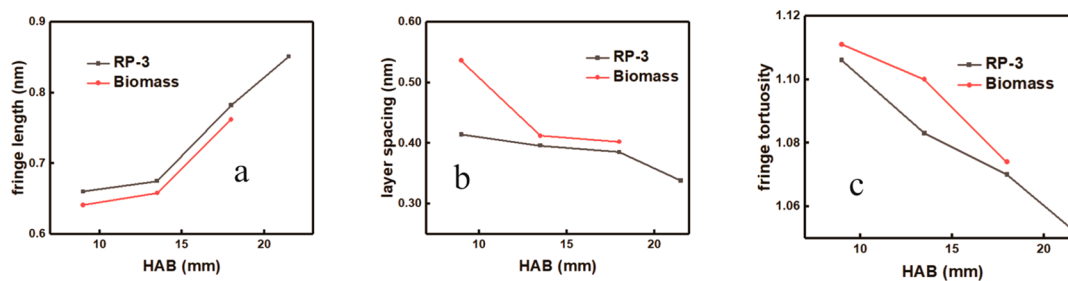
Figure 10. Nanostructure parameters ((a) fringe length (b) layer spacing, and (c) fringe tortuosity) of soot collected at different sampling points in RP-3 and biofuel flames.
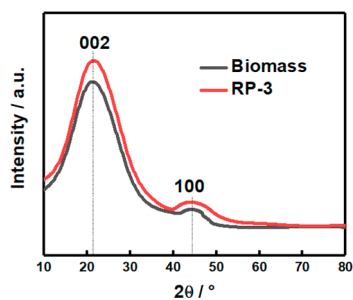
Figure 11. XRD analysis of two flame soot samples.

Table 1. Comparison of Elemental Analysis between RP-3 Soot and Biofuel Soot

sample name	C (%)	H (%)	O (%)	N (%)	H/C
RP-3	95.52	1.11	0.74	0.00	0.14
biofuel	90.78	1.66	3.09	0.00	0.22

3. CONCLUSIONS

This paper compares the evolution of the soot formation process and morphology characteristics of soot particles under free jet laminar diffusion flames between the standard jet fuel RP-3 and an algae-based biofuel. The soot particles at different flame heights are directly extracted to the TEM grid by means of probe sampling. The differences in the nanostructure characteristics of soot particles generated by the two fuel flames are compared by HRTEM, XRD, and elemental analysis. At the same time, the differences in the morphology

in the degree of graphitization. The H/C value of RP-3 soot is lower than that of biofuel soot, indicating a more organized structure. It agrees well with the previous results of HRTEM and XRD.

characteristics between RP-3 soot and biofuel soot at a lower resolution were observed by a TEM method. A probe sampling method was used to sample soot at different heights along the center axis of the flame. The differences in nanostructure characteristics of TEM, HRTEM, XRD and elemental analysis were applied to study the evolution of soot morphology and nanostructure. TEM, HRTEM, XRD and elemental analyzer were applied to analyze the soot microstructure characteristics of RP-3 soot and algae-based biofuel soot. The main research conclusions are as follows.

(1) During the growth and evolution of soot, the average particle sizes of the two types of flame soot both increase at first and then decrease due to an oxidation reaction and the surface growth of soot particles. At the flame tip, the average size of RP-3 soot particles is consistently larger than that of biofuel soot particles at the same flame height since RP-3 fuel has more aromatic radicals for PAH growth.

(2) Soot nanostructure characteristics were derived from HRTEM images processed by the software imageJ. The particles exhibit the structure of disorder with no concentric shell being detected at very low HAB. As particles travel through the flame, typical onionlike core−shell arrangements are observed with more shells of oriented stacking fringes and a smaller amorphous core. As the flame height increases, both RP-3 soot and biofuel soot exhibit a greater fringe length, a lower fringe tortuosity, and a smaller interlayer spacing, which indicates a more orderly structure. The soot of biofuel exhibits greater structural disorder with particles based on shorter fringes, more curved fringes, and a larger layer spacing of the graphene layers in comparison to that of RP-3 kerosene at the same flame height. The more disordered structure of biofuel soot indicates a higher oxidation reactivity.

(3) The results of XRD show that the 002 and 101 characteristic peaks of RP-3 soot are higher than those of biofuel soot, which indicates that RP-3 soot has more stacked carbon layers and is more stable. In an elemental analysis, RP-3 soot has a higher C/H atomic ratio in comparison to biofuel soot, which indicates that the RP-3 soot has more difficulty in being oxidized. The above conclusions are also consistent with the results of HRTEM analysis.

In this study, the evolution processes of the morphology and nanostructure of RP-3 soot and biofuel soot under a free jet diffusion flame were investigated, which may provide a comprehensive review for a further investigation of the application of alternative aviation biofuels in actual aero engines.

4. METHODS

4.1. Fuels. RP-3 is the most common commercial aviation kerosene in China with multiple components, and these components have been detailed in a prior study.[40] The algae-based biofuel, which can be hydrotreated from algae lipids by a hydrogenation process, has attracted a great deal of attention recently. Detailed components of biofuels are given in a previous study.[37] Table 2 gives the main components and contents of RP-3 kerosene and algae-based biofuel.

4.2. Experimental Setup. The schematic diagram of the experimental setup in this paper is shown in Figure 12. It

Table 2. Main Components and Contents of RP-3 Kerosene and Algae-Based Biofuel

species	amount (%)		
	saturated hydrocarbon and olefin	aromatic	others
RP-3 kerosene	54.3	28.6	17.1
hydrotreated biofuels	87.4	10.5	2.1
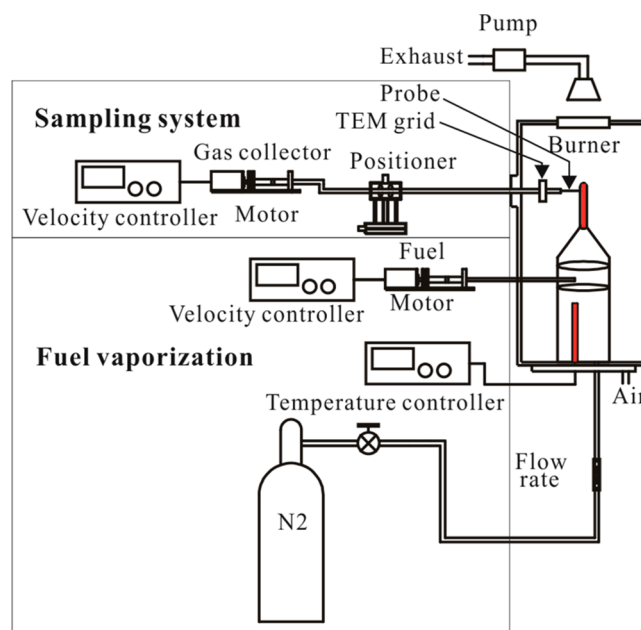
Figure 12. Schematic diagram of the experimental device.

consists of three parts: a fuel evaporation system, a burner, and a soot collection system. The fuel evaporation system is shown in the bottom left corner in Figure 12. The liquid hydrocarbon fuels RP-3 and algae-based biofuel are pre-evaporated to 673 K in the burner by a heating device attached to the inner wall of the burner. A temperature controller is equipped to control the temperature. During this process, nitrogen with a certain velocity is used as a transport carrier gas to carry the fuel vapors through the fuel nozzle. Both the RP-3 fuel and algae-based biofuel are ejected with a syringe controlled by a velocity motor. The volume flow rate of the RP-3 fuel and biomass fuel was set at 0.166 mL/min corresponding to the mass flow rates 0.129 and 0.125 g/min, respectively. The volume flow rate of nitrogen was 100 mL/min, and nitrogen was kept at room temperature. The pressure of the experiments was that of an ambient atmosphere. The burner nozzle has a 6 mm inner diameter.

4.3. Soot sampling. *4.3.1. Probe sampling.* A soot collection system was designed that was mainly based on a laboratory-made probe sampling method, which is shown in the top left corner marked with a box in Figure 12. The sampling probe was a corundum tube due to no catalytic effects on the reacting intermediate product. The inner diameter and the thickness of the corundum tube were both 1 mm. The combustion gas was drawn into a syringe uniformly pulled by an electric motor to create negative pressure. A TEM grid sealed by two PTFE membranes (shown in Figure 13) was used to filter and collect particles. A three-dimensional positioner was used for adjusting an appropriate sampling location with a resolution of 0.1 mm.
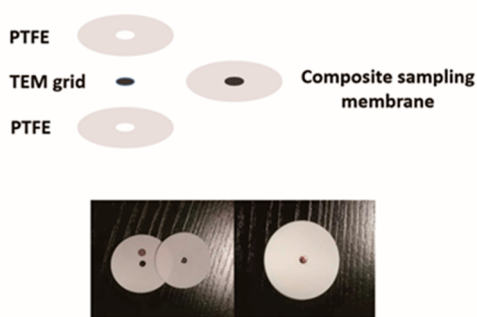
Figure 13. Composite sampling membrane.

Figure 15. Sampling points along the flame centerline.

In comparison with thermophoretic sampling, probe sampling can realize continuous sampling due to the high temperature resistance in probe sampling. However, due to the limitation of the exposure times of the probe in the flame via the thermophoretic sampling method,[41] it is difficult to collect high enough soot samples for nanostructure analysis at a very low soot concentration on the TEM grids. When the probe of thermophoresis sampling extends into the flame, it will cause a disturbance of the upstream airflow and hence a distortion of the entire flame shape. When the probe of probe sampling extends into the flame, it will not affect the upstream airflow, so that the flame shape remains relatively stable. The stability of the upstream airflow has a great effect on the accuracy of the soot sampling. Figure 14 shows the original flame shape and the flame shape when the probe is inserted into it by using probe sampling.

Figure 14. Original flame shape and the flame shape when the probe is inserted into it by using probe sampling.

4.3.2. Sampling Positions. In this investigation, the flame heights of RP-3 and biofuel were 21.5 and 18.0 mm, respectively. In order to study the changes of soot growth process in the flame, the sampling points were obtained at 4.5, 9.0, 13.5, and 18.0 mm heights above the burner (HABs) for both fuel flames. In addition, the tip of the RP-3 flame (21.5 mm HAB) was utilized as a sampling point position to ensure the integrity of the sampled data. Sampling points along the flame centerline are shown in Figure 15. The reason four or five sampling positions were selected in the experiment was to capture the growth process of soot particles during the combustion process. Then the particle samples were used for TEM, XRD, and elemental analysis.

4.4. Transmission Electron Microscopy and Image Processing. A high-resolution electron microscopy image of the soot particles can be obtained by an HRTEM analysis. The acceleration voltage of the transmission electron microscope in this experiment is 200 kV. Due to the inhomogeneity and randomness of the combustion process in time and space, the concentration of soot particles in the flame is also uneven in
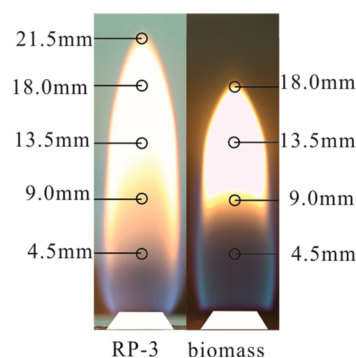
time and space. At least five images were selected for each sampling point, and more than 200 soot particles were calculated at each sampling point. Through image postprocessing and a statistical analysis of data, the parameters of the nanostructure characteristics of soot particles can be derived.

The HRTEM images were postprocessed to transform into skeletonized images by the professional image processing software imageJ. The processing steps can be summarized as follows: (1) selection of the region(s) of interest (ROI), (2) enhancement of the image contrast through a built-in function in imageJ, (3) image transformation by a Gaussian low-pass filter and bottom-hat conversion, (4) binarization (threshold by Otsu's method), (5) image skeletonization image skeletonization continuing to thin the binarized image pixels until the carbon layer is turned into a single-pixel connected image (skeletonized images are more conductive to subsequent data analysis), and (6) removal of short fringes that lack physical meaning. More detailed steps can be found in a previous report by Yehliu et al.[31]

The nanostructure parameters such as fringe length, fringe tortuosity, and interlayer spacing can be extracted from the skeletonized images. As shown in Figure 16, fringe length
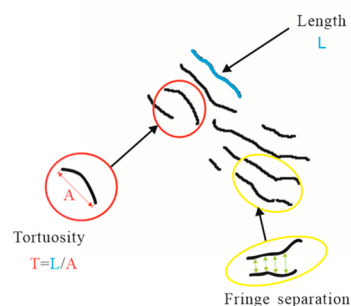
Figure 16. Particle nanostructure parameters.

refers to the actual crystallite length of the carbon layer planes. Layer spacing refers to an average value of the distance between adjacent carbon layers. Fringe tortuosity refers to the ratio of the actual physical length of the carbon layer to the linear distance between the two ends of the carbon layer.

In addition, information on the crystal properties of the soot particles was supplied by X-ray diffraction (D/MAX-2500).

■ **AUTHOR INFORMATION**

Corresponding Author

Zhiwen Gan − *National Key Laboratory of Science and Technology on Aero-engine Aero-thermodynamics, Beihang*

University, Beijing 100191, People's Republic of China;
orcid.org/0000-0003-1904-660X; Email: 09651@
buaa.edu.cn

Authors

Di Chang − National Key Laboratory of Science and
Technology on Aero-engine Aero-thermodynamics, Beihang
University, Beijing 100191, People's Republic of China;
orcid.org/0000-0002-4967-8993

Jiacheng Li − National Key Laboratory of Science and
Technology on Aero-engine Aero-thermodynamics, Beihang
University, Beijing 100191, People's Republic of China

Yiyang Yang − National Key Laboratory of Science and
Technology on Aero-engine Aero-thermodynamics, Beihang
University, Beijing 100191, People's Republic of China

Complete contact information is available at:
https://pubs.acs.org/10.1021/acsomega.1c05125

Notes

The authors declare no competing financial interest.

■ REFERENCES

(1) Vo Hoang Nhat, P.; Ngo, H. H.; Guo, W. S.; Chang, S. W.;
Nguyen, D. D.; Nguyen, P. D.; Bui, X. T.; Zhang, X. B.; Guo, J. B. Can
algae-based technologies be an affordable green process for biofuel
production and wastewater remediation? Bioresour. Technol. 2018,
256, 491−501.

(2) Cheng, F.; Luo, H. Evaluating the minimum fuel selling price of
algae-derived biofuel from hydrothermal liquefaction. Bioresour.
Technol. Rep. 2021, 100901.

(3) Glassman, I. Soot formation in combustion processes.
Symposium (International) on Combustion 1989, 22, 295−311.

(4) Sun, M.; Gan, Z.; Yang, Y. A comparison study of soot precursor
and aggregate property between algae-based aviation biofuel and
aviation kerosene rp-3 in laminar flame. Journal of Energy Resources
Technology, Transactions of the ASME 2021, 143, 112304.

(5) Mahmoud, N. M.; Yan, F.; Zhou, M.; Xu, L.; Wang, Y. Coupled
Effects of Carbon Dioxide and Water Vapor Addition on Soot
Formation in Ethylene Diffusion Flames. Energy Fuels 2019, 33,
5582−5596.

(6) Ghiassi, H.; Toth, P.; Jaramillo, I. C.; Lighty, J. S. Soot oxidation-
induced fragmentation: Part 1: The relationship between soot
nanostructure and oxidation-induced fragmentation. Combust. Flame
2016, 163, 179−187.

(7) Zhang, Y.; Zhang, R.; Kook, S. Nanostructure Analysis of In-
flame Soot Particles under the Influence of Jet-Jet Interactions in a
Light-Duty Diesel Engine. SAE International Journal of Engines 2015,
8, 2213−2226.

(8) Toth, P.; Palotas, A. B.; Ring, T. A.; Eddings, E. G.; Vander Wal,
R.; Lighty, J. S. The effect of oxidation pressure on the equilibrium
nanostructure of soot particles. Combust. Flame 2015, 162, 2422−
2430.

(9) Apicella, B.; Pré, P.; Alfè, M.; Ciajolo, A.; Gargiulo, V.; Russo,
C.; Tregrossi, A.; Deldique, D.; Rouzaud, J. N. Soot nanostructure
evolution in premixed flames by High Resolution Electron Trans-
mission Microscopy (HRTEM). Proceedings of the Combustion
Institute 2015, 35, 1895−1902.

(10) Ma, Z.; Li, L.; Chao, Y.; Kang, N.; Xu, B.; Wu, J. Effects of
Diesel Oxidation Catalyst on Nanostructure and Reactivity of Diesel
Soot. Energy Fuels 2014, 28, 4376−4382.

(11) Zhang, D.; Ma, Y.; Zhu, M. Nanostructure and oxidative
properties of soot from a compression ignition engine: The effect of a
homogeneous combustion catalyst. Proceedings of the Combustion
Institute 2013, 34, 1869−1876.

(12) Trubetskaya, A.; Jensen, P. A.; Jensen, A. D.; Garcia Llamas, A.
D.; Umeki, K.; Gardini, D.; Kling, J.; Bates, R. B.; Glarborg, P. Effects
of several types of biomass fuels on the yield, nanostructure and
reactivity of soot from fast pyrolysis at high temperatures. Applied
Energy 2016, 171, 468−482.

(13) Kholghy, M.; Saffaripour, M.; Yip, C.; Thomson, M. J. The
evolution of soot morphology in a laminar coflow diffusion flame of a
surrogate for Jet A-1. Combust. Flame 2013, 160, 2119−2130.

(14) Apicella, B.; Ciajolo, A.; Tregrossi, A.; Abrahamson, J.; Vander
Wal, R. L.; Russo, C. HRTEM and EELS investigations of flame-
formed soot nanostructure. Fuel 2018, 225, 218−224.

(15) Liati, A.; Schreiber, D.; Alpert, P. A.; Liao, Y.; Brem, B. T.;
Corral Arroyo, P.; Hu, J.; Jonsdottir, H. R.; Ammann, M.;
Dimopoulos Eggenschwiler, P. Aircraft soot from conventional fuels
and biofuels during ground idle and climb-out conditions: Electron
microscopy and X-ray micro-spectroscopy. Environ. Pollut. 2019, 247,
658−667.

(16) Blakey, S.; Rye, L.; Wilson, C. W. Aviation gas turbine
alternative fuels: A review. Proceedings of the Combustion Institute
2011, 33, 2863−2885.

(17) Li, Q.; Wang, L.; Yan, Z.; Liu, H.; Huang, Z. Effects of CO/
H2/N2 addition on the soot morphology and nanostructure in
laminar co-flow ethylene diffusion flame. Journal of the Energy Institute
2021, 95, 8−17.

(18) Karataş, A. E.; Gigone, B.; Gülder, Ö. L. Soot aggregate
morphology deduced from thermophoretic sampling in coflow
laminar methane diffusion flames at pressures up to 30 bar. Combust.
Flame 2020, 222, 411−422.

(19) Han, W.; Ya, Y.; Chu, H.; Cao, W.; Yan, Y.; Chen, L.
Morphological evolution of soot emissions from a laminar co-flow
methane diffusion flame with varying oxygen concentrations. Journal
of the Energy Institute 2020, 93, 224−234.

(20) Chu, H.; Han, W.; Cao, W.; Gu, M.; Xu, G. Effect of methane
addition to ethylene on the morphology and size distribution of soot
in a laminar co-flow diffusion flame. Energy 2019, 166, 392−400.

(21) Hu, X.; Yu, Z.; Chen, L.; Huang, Y.; Zhang, C.; Salehi, F.;
Chen, R.; Harrison, R. M.; Xu, J. Morphological and nanostructure
characteristics of soot particles emitted from a jet-stirred reactor
burning aviation fuel. Combust. Flame 2022, 236, 111760.

(22) Qiu, L.; Cheng, X.; Li, Z.; Wu, H. Experimental and numerical
investigation on soot volume fractions and number densities in non-
smoking laminar n-heptane/n-butanol coflow flames. Combust. Flame
2018, 191, 394−407.

(23) Li, Z.; Qiu, L.; Cheng, X.; Li, Y.; Wu, H. The evolution of soot
morphology and nanostructure in laminar diffusion flame of surrogate
fuels for diesel. Fuel 2018, 211, 517−528.

(24) Vander Wal, R. L.; Tomasek, A. J. Soot nanostructure:
dependence upon synthesis conditions. Combust. Flame 2004, 136,
129−140.

(25) Vander Wal, R. L.; Tomasek, A. J. Soot oxidation. Combust.
Flame 2003, 134, 1−9.

(26) Vander Wal, R. L.; Tomasek, A. J.; King, J. D. A method for
structural characterization of the range of cylindrical nanocarbons:
Nanotubes to nanofibers. Carbon 2005, 43, 2918−2930.

(27) Alfè, M.; Apicella, B.; Barbella, R.; Rouzaud, J. N.; Tregrossi, A.;
Ciajolo, A. Structure-property relationship in nanostructures of young
and mature soot in premixed flames. Proceedings of the Combustion
Institute 2009, 32, 697−704.

(28) Pan, M.; Wang, Y.; Wei, J.; Huang, H.; Zhou, X. Impact of
carbon chain length of alcohols on the physicochemical properties
and reactivity of exhaust soot. Sci. Total Environ. 2021, 799, 149434.

(29) Vander Wal, R. L.; Mueller, C. J. Initial investigation of effects
of fuel oxygenation on nanostructure of soot from a direct-injection
diesel engine. Energy Fuels 2006, 20, 2364−2369.

(30) Alfè, M.; Apicella, B.; Rouzaud, J. N.; Tregrossi, A.; Ciajolo, A.
The effect of temperature on soot properties in premixed methane
flames. Combust. Flame 2010, 157, 1959−1965.

(31) Yehliu, K.; Vander Wal, R. L.; Boehman, A. L. Development of an HRTEM image analysis method to quantify carbon nanostructure. *Combust. Flame* **2011**, *158*, 1837−1851.

(32) Oberlin, A. Carbonization and graphitization. *Carbon* **1984**, *22*, 521−541.

(33) Savic, N.; Rahman, M. M.; Miljevic, B.; Saathoff, H.; Naumann, K. H.; Leisner, T.; Riches, J.; Gupta, B.; Motta, N.; Ristovski, Z. D. Influence of biodiesel fuel composition on the morphology and microstructure of particles emitted from diesel engines. *Carbon* **2016**, *104*, 179−189.

(34) Botero, M. L.; Chen, D.; González-Calera, S.; Jefferson, D.; Kraft, M. HRTEM evaluation of soot particles produced by the non-premixed combustion of liquid fuels. *Carbon* **2016**, *96*, 459−473.

(35) Russo, C.; Alfè, M.; Rouzaud, J.-N.; Stanzione, F.; Tregrossi, A.; Ciajolo, A. Probing structures of soot formed in premixed flames of methane, ethylene and benzene. *Proceedings of the Combustion Institute* **2013**, *34*, 1885−1892.

(36) Chang, Q.; Gao, R.; Li, H.; Yu, G.; Wang, F. Effect of CO2 on the characteristics of soot derived from coal rapid pyrolysis. *Combust. Flame* **2018**, *197*, 328−339.

(37) Shi, Z.; Zhao, B.; Tang, S.; Yang, X. Hydrotreating lipids for aviation biofuels derived from extraction of wet and dry algae. *Journal of Cleaner Production* **2018**, *204*, 906−915.

(38) Abián, M.; Jensen, A. D.; Glarborg, P.; Alzueta, M. U. Soot Reactivity in Conventional Combustion and Oxy-fuel Combustion Environments. *Energy Fuels* **2013**, *27*, 2858−2858.

(39) Salamanca, M.; Velásquez, M.; Mondragón, F.; Santamaría, A. Variations of the Soot Precursors Chemical Composition Induced by Ethanol Addition to Fuel. *Energy Fuels* **2012**, *26*, 6602−6611.

(40) Zhou, T. Y.; Li, J. H.; Tan, R. Q.; Gan, Z. W.; Yang, X. Y. Impact of heptadecane and octadecane on physical properties and SMD of kerosene. *Hangkong Dongli Xuebao/Journal of Aerospace Power* **2016**, *31*, 1133−1141.

(41) Botero, M. L.; Akroyd, J.; Chen, D.; Kraft, M.; Agudelo, J. R. On the thermophoretic sampling and TEM-based characterisation of soot particles in flames. *Carbon* **2021**, *171*, 711−722.